NIS
PSE UASA
7N-34-TM
J...'3

Circular-to-Rectangular Transition Duct Flow Without and with Inlet Swirl

B. A. Reichert, W. R. Hingst, T. H. Okiishi

Circular-to-Rectangular Transition Duct Flow Without and with Inlet Swirl

Bruce A. Reichert* and Warren R. Hingst*
NASA Lewis Research Center, Cleveland, Ohio 44135
and
Theodore H. Okiishi†
Iowa State University, Ames, Iowa 50011

Circular-to-rectangular transition ducts are used as exhaust system components of aircraft with rectangular exhaust nozzles. Often, the flow into these ducts includes a swirling velocity component remaining from the gas turbine engine. Previous transition duct studies involving detailed experimental measurements have not compared the flowfield without and with inlet swirl. The study reported in this article explored circular-to-rectangular transition duct flows without and with inlet swirl in order to document the effect of inlet swirl on the transition duct flowfield and to provide detailed duct flow data for comparison with numerical code predictions. A method was devised to develop a swirling, solid-body rotational flow with minimal associated disturbances. Coefficients based on velocities and total and static pressures measured in cross-stream planes at four axial locations within the transition duct, along with surface static pressure measurements and surface oil-film visualization, are presented and discussed for both nonswirling and swirling incoming flows. In both cases the inlet centerline Mach number was 0.35. The differences between flowfields for the two cases were striking. Two pairs of counter-rotating side-wall vortices appeared in the duct flow without inlet swirl. These vortices were absent in the swirling incoming flow case.

Nomenclature

C_p = static pressure coefficient
C_{p_0} = total pressure coefficient
c = sonic velocity
D = transition duct inlet diameter
M = normalized Mach vector
M_{cl} = centerline Mach number at $x/D = -0.5$
n = exponent in Eq. (1)
p = static pressure
p_{wall} = surface static pressure at $x/D = -0.5$
p_0 = total pressure
$p_{0,cl}$ = centerline total pressure at $x/D = -0.5$
R = transition duct inlet radius
Re_D = Reynolds number
r = radial distance from duct centerline
r_y, r_z = radii in Eq. (1)
Tu = turbulence intensity
u, v, w = Cartesian velocity components
V = velocity vector
V_{cl} = velocity magnitude at the swirl generator centerline
x, y, z = Cartesian coordinates
δ^* = boundary-layer displacement thickness
ϕ = swirl angle
ϕ_{max} = maximum ideal swirl angle
Ω = angular velocity of solid-body rotation

Introduction

R ECTANGULAR exhaust nozzles offer advantages over conventional axisymmetric nozzles for aircraft. For instance, the two-dimensional/convergent-divergent nozzle described by Stevens et al.[1] is a rectangular nozzle designed to allow thrust vectoring and reversal, along with jet and expansion area variation. Enhanced mixing, which results in a cooler exhaust with less infrared emission is another benefit of rectangular nozzles.[2] Rectangular exhaust nozzles require a circular-to-rectangular transition duct to connect the engine and nozzle.

In typical exhaust component applications, the flow entering the circular-to-rectangular transition duct is turbulent, subsonic, and it often includes a significant tangential velocity component. The term swirl refers to this tangential velocity component which remains from the engine turbine. Representative studies of turbine exit flow angles[3-5] have shown that swirl often exists at turbine design operating conditions, and may be as great as 30 deg or more at off-design operating conditions. Inlet swirl can significantly influence the flowfield throughout the transition duct. Swirl has also been shown to further enhance the mixing of the flow exiting from a rectangular nozzle.[6]

A few researchers have already experimentally explored the nature of flow in circular-to-rectangular transition ducts. Patrick and McCormick[7] recorded values of total pressure, mean velocity, and three normal Reynolds stress components at the inlet and exit planes of two different circular-to-rectangular transition ducts. Miau et al.[8] measured mean velocities and turbulence intensities at the inlet and exit of three circular-to-rectangular transition ducts. In a benchmark study, Davis and Gessner[9] measured static pressures, mean velocities, and all six Reynolds stress components in three cross-stream planes within a circular-to-rectangular transition duct. Each of these studies involved incompressible flow without inlet swirl.

A limited number of transition duct studies have included the effects of inlet swirl. Der et al.[10] used water channel flow visualization to study the flow in a circular-to-rectangular tran-

sition duct with inlet swirl. Burley and Carlson[11] tested five circular-to-rectangular transition ducts including one with swirl vanes installed upstream of the duct inlet. All of these measurements were, however, limited to values of surface static pressure, thrust ratio performance parameter, and discharge coefficient. Sobota and Marble[12] made detailed measurements of the flowfield at the exit of an annular-to-rectangular transition duct. Their study included three cases of inlet swirl, but did not include a comparison with the flow without inlet swirl.

The objectives of the research described in this article were 1) to ascertain the effect of inlet swirl on a circular-to-rectangular transition duct flowfield by acquiring flowfield measurements within the duct for flows without and with inlet swirl; and 2) to provide a set of detailed experimental data for validating numerical code predictions of transition duct flows without and with inlet swirl.

A new method for swirl generation was employed to add a swirling velocity component to the flow just upstream of the transition duct. The intent of the swirl generator was to develop an approximate solid-body rotational flow free of wakes and other disturbances.

Coefficients based on detailed measurements of velocity, total pressure, and static pressure acquired in four cross-stream planes within a circular-to-rectangular transition duct, without and with inlet swirl are presented and discussed. Surface static pressure and surface oil-film visualization results are also shown and analyzed for duct flow without and with inlet swirl.

Experimental Facilities

Circular-to-Rectangular Transition Duct

Figure 1 shows the lower half of the circular-to-rectangular transition duct and the Cartesian coordinate system used throughout this article. The x axis was coincident with the duct centerline and the y and z axes were parallel to the major and minor axes of the duct exit. All coordinates were normalized with the duct inlet diameter, which was 20.42 cm. In the yz plane through each cross section, the surface of the duct satisfied Eq. (1) where the parameters r_y, r_z, and n specified the exact cross-sectional shape and varied with the axial distance x. The circular-to-rectangular ducts studied in Refs. 7 and 11 were also defined by Eq. (1) with different parameter values. The geometry of the transition duct studied in Ref. 9 was identical to the duct used in this study:

$$(y/r_y)^n + (z/r_z)^n = 1 \qquad (1)$$

In the circular region ($n = 2$), at $x/D \leq 1.0$, the duct maintained a constant circular cross section. The duct cross section was constant and nearly rectangular in the rectangular region ($n = 10$), at $x/D \geq 2.5$. The cross-sectional shape of the transition duct became more rectangular as the value of the exponent n increased from 2 to 10, but it was never truly rectangular. This was done to provide the rounded duct corners required by some CFD methods. The duct cross section changed from circular to nearly rectangular in the transition region, from $1.0 \leq x/D \leq 2.5$. The aspect ratio of the duct, defined as the ratio of the major and minor axes lengths in the rectangular cross section region, was 3.0. The transition region length-to-diameter ratio was 1.5.
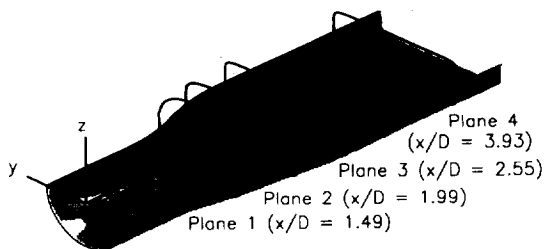

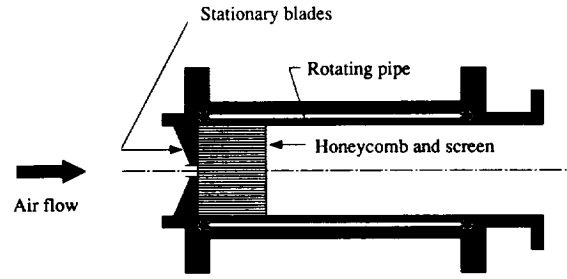Fig. 1   Circular-to-rectangular transition duct.

Fig. 2   Swirl generator schematic.

In the transition and rectangular regions of the duct it is convenient to refer to the duct surfaces normal to the y axis as the side walls, and the surfaces normal to the z axis as the top and bottom walls. The cross-sectional areas in the circular and rectangular regions were equal. In the transition region the cross-sectional area increased to 1.15 times the area in the circular and rectangular regions.

Swirl Generator

The function of the swirl generator was to superimpose a tangential velocity on the developing pipe flow. The distribution of tangential velocity sought was a forced vortex or solid-body rotation, where the tangential velocity is proportional to distance from the centerline. Figure 2 shows a schematic diagram of the swirl generator that was conceived, designed, and constructed for this study. This generator employed both stationary blades and a rotating pipe. The stationary blades produced a near solid-body rotational flow with an angular velocity that depended on the axial velocity magnitude and the blade camber angle. The honeycomb and screen were fixed to the rotating pipe and these components rotated as one assembly. The honeycomb served as a rotor that drove the rotating pipe. Additionally, the honeycomb reinforced the near solid-body rotation initiated by the stationary blades and dissipated the wakes of the stationary blades. A screen was located downstream of the honeycomb to dissipate the wakes of the honeycomb. The final section of the swirl generator was the stationary exit section. This section functioned as a stationary component to which the transition duct was attached.

ϕ is the angle of the flow from the axial direction (x axis), which varies with distance from the centerline. ϕ_{max} is an approximation of the swirl angle at the rotating pipe wall in the absence of actual boundary-layer deceleration of the axial velocity component. It is given by Eq. (2). For the results presented in this article, ϕ_{max} was 15.6 deg. Additional details about the swirl generator design, construction, operation, and performance are contained in Ref. 13:

$$\phi_{max} = \arctan(\Omega R/V_{cl}) \qquad (2)$$

Test Facility

The tests were conducted at the NASA Lewis Research Center using the internal fluid mechanics facility. Air was supplied from the test cell to a large settling chamber containing honeycomb and screens and an axisymmetric contraction having an area ratio of 59:1. The flow passed from the contraction through either a straight pipe to provide a nonswirling incoming flow to the transition duct, or the swirl generator to provide a swirling incoming flow. After passing through the transition duct, the flow was exhausted into a discharge plenum which was continuously evacuated by central exhauster facilities. Test conditions were established by regulating a mass flow valve located between the discharge plenum and the central exhauster facilities. The flow was choked at the mass flow control valve, assuring stable test conditions, unaffected by small pressure variations in the central exhauster equipment. A complete description of the internal fluid mechanics facility is given by Porro et al.[14]

Experimental Methods and Results

Total and static pressure results are presented as pressure coefficients, nondimensionalized as indicated in Eqs. (3) and (4). Velocity vectors were divided by the local c to yield a Mach vector and then normalized by the centerline Mach number, as shown in Eq. (5). Bold type in Eq. (5) indicates vector quantities. In subsequent discussion the quantities defined by Eqs. (3-5) are referred to simply as total pressure, static pressure, and velocity. In Eqs. (3-5), the reference variables subscripted cl (centerline, $r = 0$) or wall ($r = R$) were evaluated at a location one radius upstream of the transition duct inlet ($x/D = -0.5$). This location is near the exit of the straight pipe or swirl generator:

$$C_{p_0} = \frac{p_0 - p_{wall}}{p_{0,cl} - p_{wall}} \tag{3}$$

$$C_p = \frac{p - p_{wall}}{p_{0,cl} - p_{wall}} \tag{4}$$

$$M = \frac{V/c}{M_{cl}} = \left(\frac{u/c}{M_{cl}}, \frac{v/c}{M_{cl}}, \frac{w/c}{M_{cl}} \right) \tag{5}$$

Test Conditions

Test conditions were verified by a survey of the flowfield one radius upstream of the transition duct inlet. The test conditions for the flow without and with inlet swirl are summarized in Table 1. The Reynolds number is based on the centerline velocity and the transition duct inlet diameter. The difference in Reynolds number between the two cases resulted from a total pressure loss associated with the swirl generator. Turbulence intensity was measured with a single hot-wire probe located at the centerline and oriented normal to the flow. The integral length scale, based on hot-wire autocorrelation measurements at the centerline, was estimated to be 3 mm. Turbulence intensity and length scale were not measured for flow with inlet swirl. Mass flow through the duct was 4.32 kg/s for the nonswirling case and 3.82 kg/s for the swirling case. As with Reynolds number, the change in mass flow results from total pressure loss in the swirl generator. The total temperature for all tests was test cell ambient temperature, nominally 293 K.

Table 1   Test conditions for flow without and with inlet swirl
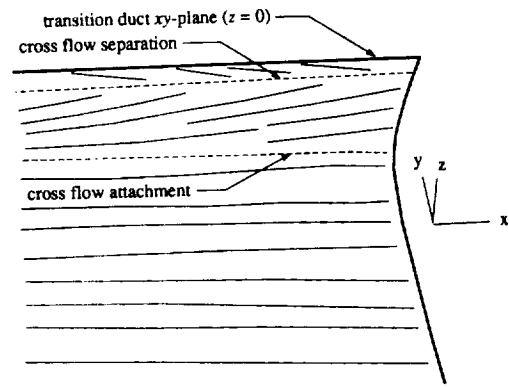
	Without inlet swirl	With inlet swirl
M_{cl}	0.35	0.35
Re_D ($\times 10^{-6}$)	1.58	1.37
ϕ_{max}	0.0 deg	15.6 deg
δ^*/D ($\times 10^2$)	0.74	2.02
Tu	0.65%	N.A.
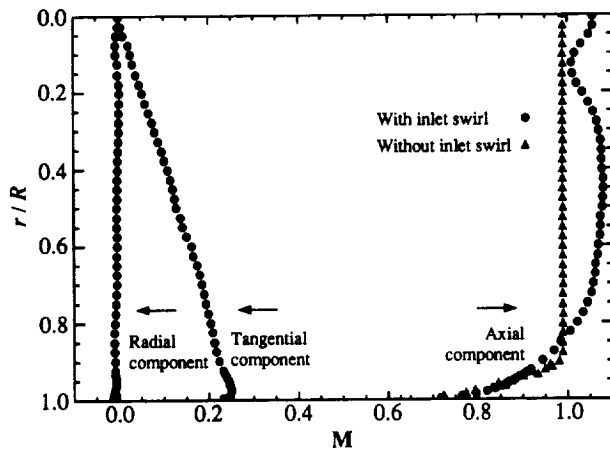
Fig. 3   Inlet velocity distribution.
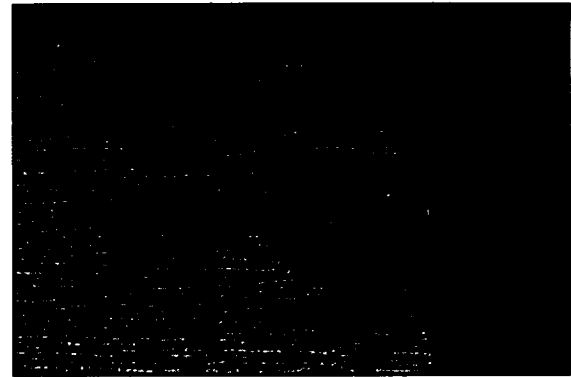
a)

b)

Fig. 4   Surface oil-film visualization for nonswirling incoming flow: a) detail showing duct side-wall near the duct exit and b) sketch and annotation of flow visualization features.

Detailed velocity data for the flow just upstream of the duct inlet are displayed in Fig. 3. There were no measurable tangential velocity components for the flow without the swirl generator in place. With the swirl generator operating, the small decrease in axial flow near the centerline is a result of the total pressure losses produced by the small centerbody used to hold the stationary swirl generator blades.
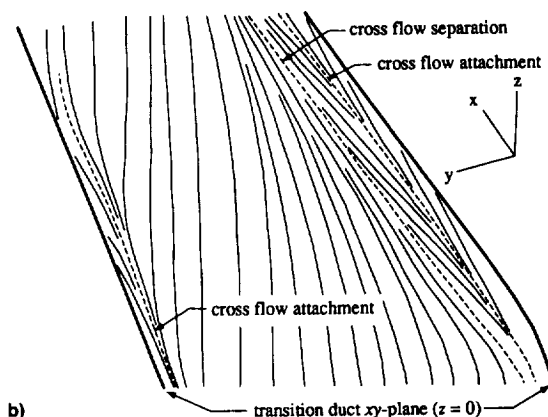
Surface Oil-Film Visualization

A surface oil-film visualization technique utilizing fluorescent dye was used to obtain information about the flowfield near the transition duct surface. Figure 4a shows surface oil-film visualization results for flow without inlet swirl. The flow is from left to right, and local coordinate system is shown to help establish the orientation of the photograph. The photograph was digitized with an image scanner and then numerically enhanced to improve the contrast. Figure 4b shows a sketch made from the digitized image where the significant features of the photograph have been labeled. The results for flow with inlet swirl are shown in Fig. 5 where the flow is from the lower right to upper left. This will be discussed in the Discussion and Conclusions section.

Surface Static Pressure Measurements

Surface static pressure measurements were made through 50 small (0.51-mm) tap holes equally spaced on the duct surface in the xz plane along the broken line shown in Fig. 1. Open symbols in Fig. 6 represent the static pressure along the lower surface of the duct for flow without and with inlet swirl. Vertical broken lines indicate the locations of the four cross-stream measurement planes. The solid symbols on these lines represent the static pressure measured at the duct centerline with a five-hole probe as explained below.

a)
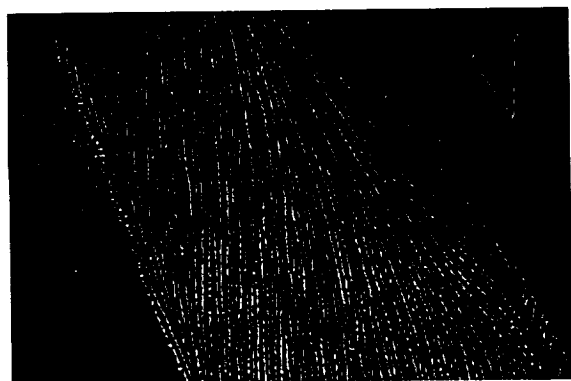
Fig. 5 Surface oil-film visualization for swirling incoming flow: a) detail showing corner near the duct exit and b) sketch and annotation of flow visualization features.
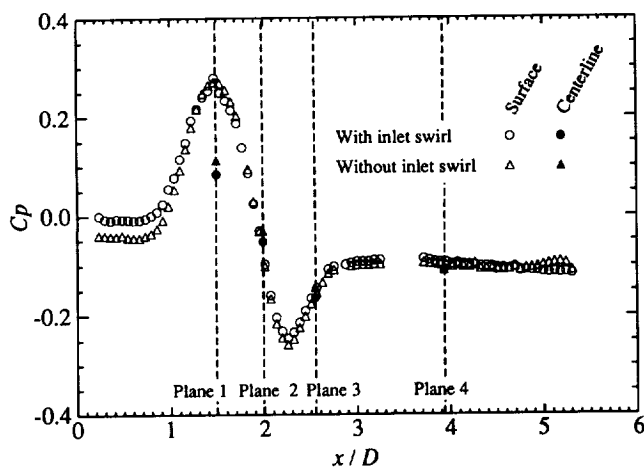

Fig. 6 Surface static pressure coefficient for flow without and with inlet swirl.

Five-Hole Probe Measurements

A calibrated five-hole probe was used to measure airflow speed, direction, total pressure, and static pressure in four cross-stream measurement planes in the transition duct. Measurements were recorded with the five-hole probe at approximately 480 locations in each measurement plane. The axial location of the four measurement planes is given in Fig. 1. The transition duct was symmetric with respect to the horizontal xy plane and the vertical xz plane. Flow without inlet swirl required measurements in only one quadrant at each measurement plane. Measurements were made in two quadrants, however, on both sides of the xz plane. The additional

measurements were made to confirm the symmetry of the transition duct flow without inlet swirl, and to provide comparison data for the swirling flow case, for which measurements in two adjacent quadrants were required.

The results of detailed surveys of the flow in the four cross-stream measurement planes are shown in Figs. 7–10. The view in Figs. 7–10 is looking downstream with the flow from left to right. The cross section of the transition duct was drawn to the same scale in each figure. Measurements were made in the lower half of the transition duct only. The data shown in the upper half of the duct in Figs. 7–10 were transformed by symmetry rules from the lower half.

Contours of the values of the axial velocity component at each measurement plane for flow without and with inlet swirl are plotted in Figs. 7a and 9a. Figure 7b and 9b show the transverse velocity components. Beneath each figure is a vector labeled M_{cl}. This is the reference length scale used for the plots of transverse velocity components. The same reference
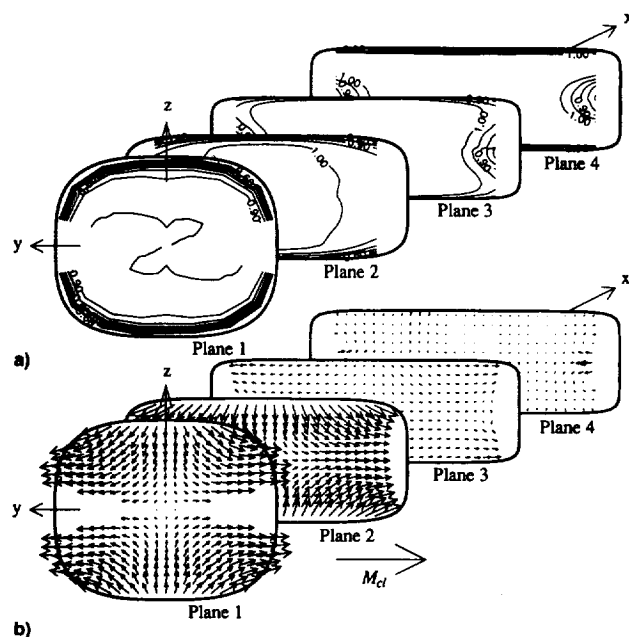

Fig. 7 a) Axial contours and b) transverse components of M for flow without inlet swirl.
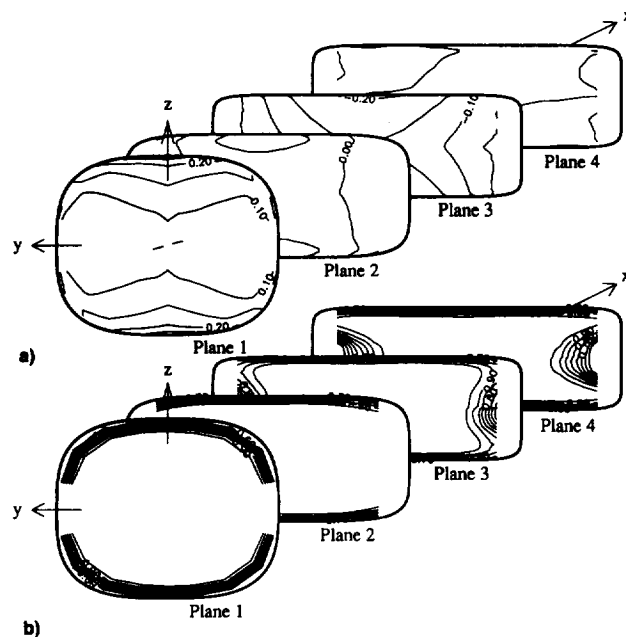

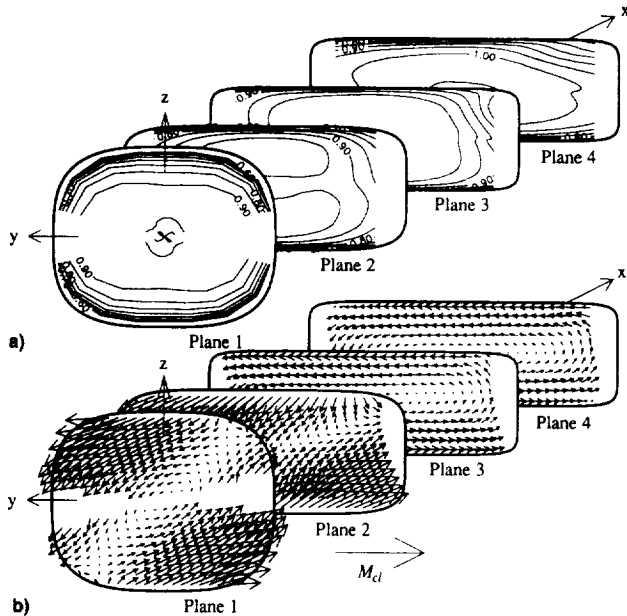**Fig. 8 Distributions for flow without inlet swirl: a) C_p and b) C_{p_0}.**

Fig. 9 a) Axial contours and b) transverse components of M for flow with inlet swirl.
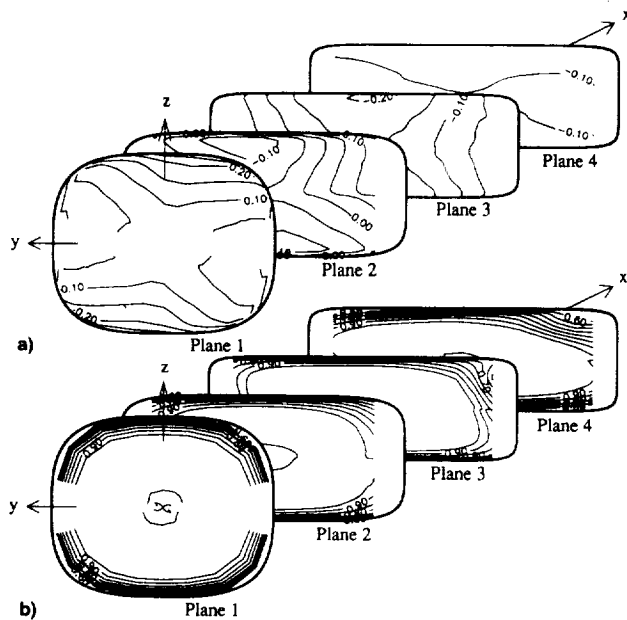

Fig. 10 Distributions for flow with inlet swirl: a) C_p and b) C_{p_0}.

length was used at each measurement plane for both figures. This allows direct comparisons to be made between results at different planes or for different inlet conditions.

Contour plots of static pressure at each measurement plane are shown in Figs. 8a and 10a. The same contour levels were used in all plots. The broken lines that appear in the static pressure contours indicate negative coefficient values. Contour plots of total pressure are shown in Figs. 8b and 10b.

Discussion and Conclusions

Flow Without Inlet Swirl

The distribution of static pressures was generally attributed to the response of the flowfield outside the boundary layer to the changing duct geometry. The change in cross section of the duct forced the flow to converge in the xz plane and diverge in the xy plane. The duct wall deflected the incoming flow, initially directed parallel to the x axis, towards the x

axis in the xz plane and away from the x axis in the xy plane. For the duct flow without inlet swirl, this initial streamline curvature produced a saddle-shaped static pressure distribution in the yz plane, with minimum static pressures near either side wall and maximum static pressures near the top and bottom walls. This static pressure distribution can be seen at plane 1 of Fig. 8. The maximum pressures are also observable as the maximum value that appears in the surface static pressure plot shown in Fig. 6.

Another saddle-shaped static pressure distribution in the yz plane was developed further downstream in the rectangular region where streamline curvature was reversed as the flow was forced by the duct wall back to a direction that was nominally parallel to the x axis. This static pressure distribution involved maximum static pressures near either end wall and minimum static pressures near the top and bottom walls. Evidence of this distribution can be seen in the static pressure distribution at plane 3 of Fig. 8 and as the minimum value of the surface static pressure plot shown in Fig. 6. Miau et al.[8] and Davis and Gessner[9] also observed this reversal of the static pressure distribution in their surface static pressure measurements.

The location of the maximum and minimum static pressures were reversed between planes 1–3 for reasons described above. In order to affect the reversal of static pressure, there must be an intermediate location where the static pressure distribution in the yz plane was nominally flat. The results show the intermediate location must be between planes 1, at $x/D = 1.49$, and 2, at $x/D = 1.99$. The static pressure distribution at plane 2 of Fig. 8 already shows the reversal of the location of the maximum and minimum static pressures, although the pressure gradients are less than those observed at plane 3. Surface static pressure measurements made by Davis and Gessner[9] around cross-stream planes in an identical duct show that the static pressure reversal occurred between $x/D = 1.60$ and $x/D = 1.90$. The overall level of static pressure was higher at planes 1 and 2 because of the increase in cross-sectional area at these measurement planes.

The static pressure distribution at plane 4 of Fig. 8 is nominally flat. The slight pressure gradients observed in the static pressure distribution probably resulted from the upstream influence of the discharge plenum at the transition duct exit ($x/D = 5.47$), which was an abrupt enlargement.

The cross-stream static pressure distribution established outside the boundary layer balances the centrifugal force produced by curved streamlines. Within the boundary layer the velocity is reduced, but the cross-stream pressure gradient imposed by the flow outside the boundary layer is not. This can result in significant flow turning in the boundary layer and is referred to as skew-induced secondary flow or crossflow.[15] The rate of crossflow production increases as the amount of streamline curvature increases. The magnitude of the crossflow increases as the distance to the wall diminishes until very near the wall where the no-slip condition is satisfied. Within the transition duct this can be seen at planes 1 and 2 of Fig. 7b, where the greatest transverse velocity components appear near the duct surface side walls where streamline curvature is greatest.

The crossflow in the boundary layer near the transition duct side walls seen in the transverse velocity plots at planes 1 and 2 in Fig. 7b resulted in two pairs of counter-rotating side-wall vortices that were clearly present at planes 3 and 4. Symmetry and continuity were the mechanisms that produced counter-rotating axial vortices from the crossflow within the transition duct. For flow without inlet swirl, the two symmetry planes of the transition duct were stream surfaces, and therefore, no flow crossed these planes. At the transition duct side walls the crossflow approached the xy plane from both above and below. Continuity redirected these crossflows approaching the xy plane away from the side walls and inwards towards the duct center. The vortex pattern was thus established. Although the transverse static pressure distribution reversed ori-

entation between planes 1 and 2, the second static pressure distribution failed to completely reverse the crossflow initiated by the first static pressure distribution.

Davis and Gessner[9] observed nearly identical behavior of the transverse velocities in their measurement planes downstream of the transition region in an identical transition duct. Patrick and McCormick[7] observed similar side-wall vortices at the exit plane of their duct with an aspect ratio of 6. The side-wall vortices were not apparent at the exit plane of their duct with an aspect ratio of 3, although crossflow in the boundary layer near the side walls was observed at the exit plane. Miau et al.[8] observed axial vorticity near the exit plane of their transition duct with an aspect ratio of 2; however, this vorticity was opposite in direction compared to the dominant side-wall vortices seen in Fig. 7.

Although pressure probe data were not acquired very near the duct side walls, the surface oil-film visualization information provides evidence of two additional pairs of vortices in this region. This can be seen in the visualization results presented in Fig. 4a. A line appears on the duct side wall approximately 0.15 radius below the xy plane. In Fig. 4b this line has been labeled "cross flow separation." Nearby lines exhibit asymptotic behavior, approaching this line from above and below resulting in a herringbone-like pattern. Figure 11a is a sketch representing the pattern of secondary flow inferred from the surface oil-film visualization information, showing the second pair of smaller vortices.

An effect of the dominant side-wall vortices observed downstream of the transition region was the convection of fluid from the boundary layer into the freestream region. This convection produced distortion in the axial velocity and total pressure contours. This is particularly apparent at plane 4 of Fig. 8b, where the low total pressure fluid, normally associated with the boundary layer, extends outward from the side walls toward the duct centerline.

Our data indicate no regions of global flow separation (characterized by reverse streamwise flow and the presence of a saddle point in the surface oil-film visualization) in the transition duct. Davis and Gessner[9] made this same observation in their study of an identical transition duct. However, local or crossflow separation (not requiring reverse streamwise flow or a saddle point) in the transition duct is clearly indicated by the side-wall vortices appearing in the transverse velocity results, the distorted contours of total pressure, and the surface oil-film visualization results.

Flow with Inlet Swirl

The effect of inlet swirl on the transition duct flowfield was complex. On one hand, there appeared to be little influence of inlet swirl on the duct surface static pressure distribution, as shown in Fig. 6. However, the difference in detailed data, in particular the transverse components of velocity, in all measurement planes for flow without and with inlet swirl is striking. For example, there is no evidence in plane 3 or 4 of Fig. 9b of the two pairs of counter-rotating side-wall vortices that were observed for flow without inlet swirl.

An important consequence of inlet swirl is its effect on the symmetry of the transition duct flowfield. The flowfield without swirl had two mutually perpendicular planes of mirror symmetry that acted like stream surfaces. These two symmetry planes which were also stream surfaces were significant in producing counter-rotating vortices from the crossflow of boundary-layer fluid. The flowfield with inlet swirl had only one plane of rotational symmetry which was not a stream surface and thus allowed through flow.

When viewed looking downstream, the incoming flow with swirl was rotating counterclockwise resulting in a region outside the wall boundary layer of nearly constant negative axial vorticity. The overwhelming fluid flow effect was that the duct geometry driven convergence in the xz plane and the divergence in the xy plane was aided by the counterclockwise swirl in the upper left and lower right quadrants, and opposed by the counterclockwise swirl in the upper right and lower left quadrants as shown in the sketch in Fig. 12.

This flow pattern established the static pressure distribution for plane 1 seen in Fig. 10a. The static pressure distribution was saddle-shaped as for the nonswirling flow; however, the regions of highest static pressure were now located near the lower left and upper right corners, and the regions of lowest static pressure were located near the lower right and upper left corners. The static pressure gradient associated with the maximum and minimum static pressures drove the boundary-layer flow near the lower left and upper right corners in two directions, some against the direction of rotation and some in the direction of rotation. This effect can be seen in the plot of transverse velocity at plane 1 of Fig. 9b. The response to the static pressure gradient was again greater in the boundary layer where the momentum was less, resulting in crossflow.

The saddle-shaped static pressure distribution observed in Fig. 10a at plane 1 persisted to plane 2; however, it was not as pronounced. The 90-deg circumferential shift of the orientation of the static pressure distribution seen in the flowfield without inlet swirl was not observed for swirling flow. Instead, the regions of highest static pressure remained in the lower left and upper right quadrants, but they appeared to be displaced clockwise, the highest static pressures being nearer to the y axis and the lowest static pressures being nearer to the z axis.

At plane 3, the static pressure distribution in Fig. 10a does not differ significantly from the nonswirling static pressure
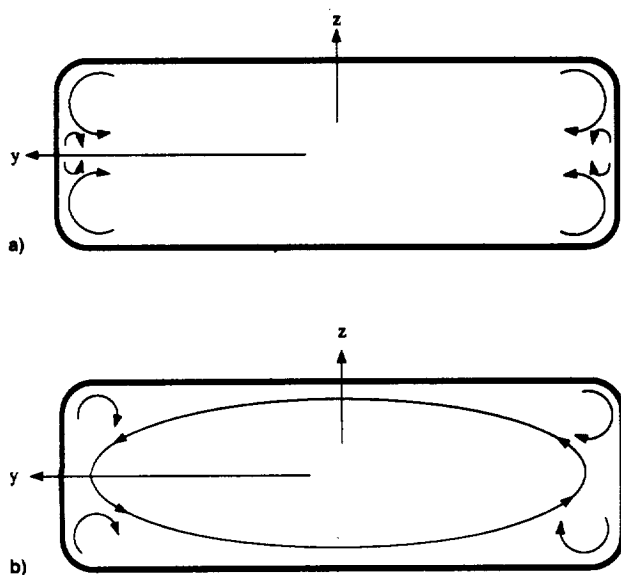

Fig. 11 The pattern of secondary flow inferred from surface oil-film visualization (view looking downstream): a) flow without inlet swirl and b) flow with inlet swirl.
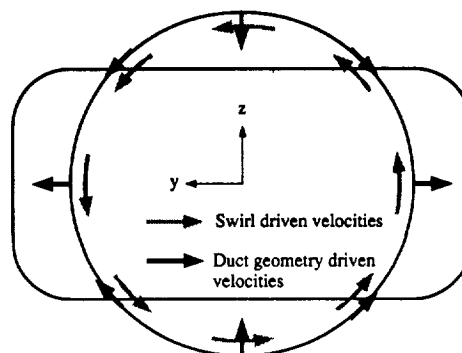

Fig. 12 Sketch of swirl driven and duct geometry driven velocities for transition duct flow with inlet swirl (view looking downstream).

distribution in the same plane (Fig. 8a). For nonswirling flow, the maximum static pressures were on the side walls and the minimum static pressures were on the top and bottom walls. The static pressure distribution changed its orientation nearly 90 deg from plane 1. The reversal of the static pressure distribution orientation for flow without inlet swirl was described earlier. For the nonswirling case, the reversal involved a cross plane of nearly constant static pressure. For the swirling case, the reversal of the static pressure distribution orientation was accomplished without a nominally flat static pressure distribution. The orientation of the static pressure distribution appeared instead to experience, in effect, a clockwise rotation.

The static pressure distribution shown in plane 4 of Fig. 10a had the same shape as the distribution in plane 3, however, the gradients were not as great. At this location and further downstream, the static pressure distribution was nearly uniform and had little effect on the boundary-layer flow.

The distortion of total pressure distribution is most apparent in the upper right and lower left quadrant in planes 3 and 4 of Fig. 10b. As in the nonswirling case, this distortion resulted from the convection of boundary-layer fluid by secondary flows. The slight depression in total pressure near the centerline that appeared in all four planes is a signature (Fig. 3) of the swirl generator centerbody.

Surface oil-film visualization results indicate the presence of vortices in each corner of the duct downstream of the transition region. Figure 5 shows lines of local or crossflow separation and attachment in each corner. A sketch of the pattern of secondary flow inferred from the surface oil-film visualization information is given in Fig. 11b. Both pressure probe measurements and surface oil-film visualization data show that these corner vortices are smaller than the primary vortex of the flowfield with swirl and the pairs of counter-rotating vortices in the flowfield without inlet swirl. In an intuitive sense, the corner vortices help "round" or "fill" the transition duct corners. All measurements indicate the absence of global separation throughout the transition duct for flow with inlet swirl.

A comparison of the experimental results at the transition duct exit for flow with inlet swirl with data from earlier studies pointed out interesting differences. The results of Der et al.[10] show that their swirling flow split into two primary corotating vortices. Also, they observed two smaller vortices in diagonally opposed corners of the duct that rotated in directions opposite from the two primary vortices. Sobota and Marble[12] made the same observation for one of the three swirl cases they studied, while the other two cases involved a strong, concentrated central vortex with two smaller vortices located at diagonally opposed sides of the central vortex. Our results show no evidence of the forced vortex swirling flow splitting into two corotating vortices. Since the earlier studies used somewhat similar duct geometries and amounts of swirl, the difference in the results suggests the importance of the kind of swirl distribution (e.g., forced or free vortex) involved.

Summary

When utilized as exhaust system components of aircraft with rectangular nozzles, the incoming flow to circular-to-rectangular transition ducts often includes a swirling velocity component remaining from the gas turbine engine. Inlet swirl significantly influences the transition duct flowfield. Outside the boundary layer, the response of the flowfield velocity to

the changing duct geometry gives rise to streamline curvature and a corresponding static pressure distribution. For nonswirling incoming flow, the static pressure distribution produced boundary-layer crossflows which evolved into two pairs of counter-rotating side-wall vortices. For the inlet swirl flow studied, the counter-rotating side-wall vortices were not observed. Inlet swirl had altered the flowfield to an extent that the side-wall vortices were suppressed. The effects of inlet swirl should be included in the design of circular-to-rectangular transition ducts for aircraft exhaust systems.

Acknowledgments

References

[1]Stevens, H. L., Thayer, E. B., and Fullerton, J. F., "Development of the Multi-Function 2-D/C-D Nozzle," AIAA Paper 81-1491, July 1981.

[2]Sforza, P. M., and Stasi, W., "Heated Three-Dimensional Turbulent Jets," *Journal of Heat Transfer*, Vol. 101, May 1979, pp. 353–358.

[3]Whitney, W. J., Schum, H. J., and Behning, F. P., "Cold-Air Investigation of a Turbine for High-Temperature-Engine Application IV—Two-Stage Turbine Performance," NASA TN D-6960, Sept. 1972.

[4]Szanca, E. M., Schum, H. J., and Hotz, G. M., "Research Turbine for High-Temperature Core Engine Application I—Cold-Air Overall Performance of Solid Scaled Turbine," NASA TN D-7557, Feb. 1974.

[5]Schwab, J. R., Stabe, R. G., and Whitney, W. J., "Analytical and Experimental Study of Flow Through Axial Turbine Stage with a Nonuniform Inlet Radial Temperature Profile," AIAA Paper 83-1175, June 1983.

[6]Chu, C. W., Der, J., Jr., Ortiz, V. M., and Widynski, T. C., "Effect of Swirl on the Potential Core in Two-Dimensional Ejector Nozzles," *Journal of Aircraft*, Vol. 20, No. 1, 1983, pp. 191, 192.

[7]Patrick, W. P., and McCormick, D. C., "Circular-to-Rectangular Duct Flows—A Benchmark Experimental Study," Society of Automotive Engineers Paper 871776, Oct. 1988.

[8]Miau, J. J., Leu, T. S., Chou, J. H., Lin, S. A., and Lin, C. K., "Flow Distortion in a Circular-to-Rectangular Transition Duct," *AIAA Journal*, Vol. 28, Aug. 1990, pp. 1447–1456.

[9]Davis, D. O., and Gessner, F. B., "Experimental Investigation of Turbulent Flow Through a Circular-to-Rectangular Transition Duct," *AIAA Journal*, Vol. 30, Feb. 1992, pp. 367–375.

[10]Der, J., Jr., Chu, C. W., Hunt, B. L., and Lorincz, D. J., "Evolution of Swirl in Two-Dimensional-Nozzle Flow," *Journal of Aircraft*, Vol. 19, No. 2, 1982, pp. 347–349.

[11]Burley, J. R., II, and Carlson, J. R., "Circular-to-Rectangular Transition Ducts for High-Aspect Ratio Nonaxisymmetric Nozzles," AIAA Paper 85-1346, July 1985.

[12]Sobota, T. H., and Marble, F. E., "Swirling Flows in an Annular-to-Rectangular Transition Section," *Journal of Propulsion and Power*, Vol. 5, No. 2, 1989, pp. 334–340.

[13]Reichert, B. A., "A Study of High Speed Flows in an Aircraft Transition Duct," Ph.D. Dissertation, Iowa State Univ., Ames, IA, March 1991; see also NASA TM 104449.

[14]Porro, A. R., Hingst, W. R., Wasserbauer, C. A., and Andrews, T. B., "The NASA Lewis Research Center Internal Fluid Mechanics Facility," NASA TM 105187, Sept. 1991.

[15]Bradshaw, P., "Turbulent Secondary Flows," *Annual Review of Fluid Mechanics*, Vol. 19, 1987, pp. 53–74.